Flybys in protoplanetary discs - II. Observational signatures

Nicolás Cuello, Fabien Louvet, Daniel Mentiplay, Christophe Pinte, Daniel J. Price, Andrew J. Winter, Rebecca Nealon, François Ménard, Giuseppe Lodato, Giovanni Dipierro, et al.

▶ To cite this version:

Nicolás Cuello, Fabien Louvet, Daniel Mentiplay, Christophe Pinte, Daniel J. Price, et al.. Flybys in protoplanetary discs - II. Observational signatures. Monthly Notices of the Royal Astronomical Society, 2020, 491, pp.504-514. 10.1093/mnras/stz2938 . insu-03705227

HAL Id: insu-03705227
https://insu.hal.science/insu-03705227

Monthly Notices
of the
ROYAL ASTRONOMICAL SOCIETY

MNRAS **491,** 504–514 (2020)
Advance Access publication 2019 October 21

doi:10.1093/mnras/stz2938

Flybys in protoplanetary discs – II. Observational signatures

Nicolás Cuello,[1,2,3]★ Fabien Louvet,[4] Daniel Mentiplay,[5] Christophe Pinte,[5,6] Daniel J. Price,[5] Andrew J. Winter,[3] Rebecca Nealon,[3] François Ménard,[6] Giuseppe Lodato,[7] Giovanni Dipierro,[3] Valentin Christiaens,[5] Matías Montesinos,[2,8,9] Jorge Cuadra,[1,2] Guillaume Laibe,[10] Lucas Cieza,[11] Ruobing Dong[12] and Richard Alexander[3]

[1]*Instituto de Astrofísica, Pontificia Universidad Católica de Chile, Santiago, Chile*
[2]*Núcleo Milenio de Formación Planetaria (NPF), Chile*
[3]*School of Physics and Astronomy, University of Leicester, University Road, Leicester LE1 7RH, UK*
[4]*Departamento de Astronomía de Chile, Universidad de Chile, Santiago, Chile*
[5]*Monash Centre for Astrophysics (MoCA) and School of Physics and Astronomy, Monash University, Clayton VIC 3800, Australia*
[6]*Univ. Grenoble Alpes, CNRS, IPAG, F-38000 Grenoble, France*
[7]*Dipartimento di Fisica, Università Degli Studi di Milano, Via Celoria, 16, I-20133 Milano, Italy*
[8]*Inst. Física y Astronomía, Fac. Ciencias, Universidad de Valparaíso, Gran Bretaña 1111, Valparaíso, Chile*
[9]*Chinese Academy of Sciences South America Center for Astronomy, National Astronomical Observatories, CAS, Beijing 100012, China*
[10]*Univ Lyon, Univ Lyon1, Ens de Lyon, CNRS, Centre de Recherche Astrophysique de Lyon UMR5574, F-69230 Saint-Genis-Laval, France*
[11]*Facultad de Ingeniería y Ciencias, Núcleo de Astronomía, Universidad Diego Portales, Av. Ejercito 441, Santiago, Chile*
[12]*Department of Physics & Astronomy, University of Victoria, Victoria, BC V8P 1A1, Canada*

Accepted 2019 October 15. Received 2019 October 11; in original form 2019 August 23

ABSTRACT

Tidal encounters in star clusters perturb discs around young protostars. In Cuello et al., we detailed the dynamical signatures of a stellar flyby in both gas and dust. Flybys produce warped discs, spirals with evolving pitch angles, increasing accretion rates, and disc truncation. Here, we present the corresponding observational signatures of these features in optical/near-infrared scattered light and (sub) millimetre continuum and CO line emission. Using representative prograde and retrograde encounters for direct comparison, we post-process hydrodynamical simulations with radiative transfer methods to generate a catalogue of multiwavelength observations. This provides a reference to identify flybys in recent near-infrared and submillimetre observations (e.g. RW Aur, AS 205, HV Tau and DO Tau, FU Ori, V2775 Ori, and Z CMa).

Key words: hydrodynamics – methods: numerical – planets and satellites: formation – protoplanetary discs.

1 INTRODUCTION

Protoplanetary discs are the cradle of newborn planets. Given typical disc lifetimes – 1 to 10 Myr – planets should form within these systems in less than a few Myr. However, despite an active search for embedded planets in protoplanetary discs, only three candidates have been reported so far: in PDS 70 (Keppler et al. 2018; Müller et al. 2018), HD 163296 (Pinte et al. 2018), and HD 97048 (Pinte et al. 2019). A complete theoretical understanding of planet formation remains elusive (Armitage 2018).

Numerous radial and azimuthal features such as spirals (Benisty et al. 2015, 2017; Pérez et al. 2016; Huang et al. 2018), shadows (Avenhaus et al. 2014; Stolker et al. 2016; Benisty et al. 2018), gaps (ALMA Partnership 2015; Tsukagoshi et al. 2016; Andrews et al. 2018; Dipierro et al. 2018), warps (Casassus et al. 2018; Langlois et al. 2018; van der Plas et al. 2019), horseshoes (van der Marel et al. 2013; Boehler et al. 2017), and clumps (Dong et al. 2018; Gratton et al. 2019) have been reported. Such structures are potential signposts of disc–companion interactions (for instance Dong et al. 2015; Price et al. 2018b; Calcino et al. 2019; Poblete, Cuello & Cuadra 2019).

Spirals and misaligned inner/outer discs are often assumed to be indicators of massive (planetary or stellar) perturbers. These companions can either be external (Clarke & Pringle 1993; Pfalzner 2003; Quillen et al. 2005; Dong et al. 2015) or internal (Facchini, Lodato & Price 2013; Lodato & Facchini 2013; Cazzoletti et al. 2017; Aly, Lodato & Cazzoletti 2018; Keppler et al. 2018; Price

---

★ E-mail: cuellonicolas@gmail.com

Published by Oxford University Press on behalf of the Royal Astronomical Society

et al. 2018b; Cuello & Giuppone 2019) to the protoplanetary disc. Interestingly, planetary companions on inclined orbits are able to warp the disc (Facchini, Ricci & Lodato 2014; Nealon et al. 2018) and produce observable features in scattered light (Nealon et al. 2019; Zhu 2019). Massive companions may also lead to disc breaking with observational signatures present in both scattered light and mm wavelengths (Facchini, Juhász & Lodato 2018; Montesinos & Cuello 2018; Cuello et al. 2019b). Additionally, accretion from an external envelope (Harsono, Alexander & Levin 2011; Lesur, Hennebelle & Fromang 2015; Hennebelle, Lesur & Fromang 2017) and chaotic interactions within a molecular cloud (Bate, Lodato & Pringle 2010; Bate 2018) can also form spirals and misaligned discs. In this work, we focus on the scenario where a disc is perturbed by a stellar companion on an unbound (parabolic) orbit. Our aim is to predict the resulting observational signatures.

Parabolic star–disc encounters are expected to occur during the early phases of stellar evolution (<1 Myr) in clustered associations of stars (Craig & Krumholz 2013; Pfalzner 2013; Winter et al. 2018b). It is therefore likely that at least one of the stars involved in the encounter has a protoplanetary disc. Signatures of such encounters have been observed, e.g. in RW Aur (Dai et al. 2015; Rodriguez et al. 2018), HV & DO Tau (Winter, Booth & Clarke 2018c), FU Ori (Takami et al. 2018), and AS 205 (Kurtovic et al. 2018). Provided the encounter is close enough, the stellar flyby can dramatically affect the disc structure creating spirals, bridges, warps, and diffuse nebulae. In a previous study (Cuello et al. 2019a, hereafter Paper I), we examined the dynamical signatures of flybys in the gas and in the dust.

Our aim in this paper is to provide observational diagnostics of protoplanetary discs experiencing a stellar flyby. We investigate the disc emission at different wavelengths as a function of orbital inclination of the flyby. In Section 2, we describe the methodology followed to perform the radiative transfer calculation and the corresponding synthetic observations. In Section 3, we classify the flyby signatures at different wavelengths in order to provide a guide to interpret recent observations. Our results are discussed in the light of recent observations of interacting stellar objects in Section 4. We conclude in Section 5.

2 METHODS

In Paper I, we presented a series of smoothed particle hydrodynamical (SPH) simulations of a protoplanetary disc disturbed by a single stellar flyby. We used PHANTOM (Price et al. 2018a). Calculations were performed for a range of orbital (prograde and retrograde) inclinations and grain sizes (Section 2.1). The response of the protoplanetary disc to the gravitational perturbation of the intruder depends on the orbital inclination and stellar mass ratio. For instance, disc truncation is more efficient for prograde encounters; whereas disc warping is greater in retrograde encounters (Xiang-Gruess 2016). Both effects increase with increasing pertuber-to-host mass ratio, q. Here, we characterize the observational signatures of those encounters by post-processing the hydrodynamical simulations with MCFOST (Pinte et al. 2006, 2009), see radiative transfer calculations in Section 2.2.

2.1 Disc model and flyby parameters

We considered a $1\,\mathrm{M}_\odot$ star surrounded by a protoplanetary disc with mid-plane initially in the xy- (or equivalently $z = 0$) plane. We set-up a disc with an initial inner and outer disc radius of $R_{\rm in} = 10$ au and $R_{\rm out} = 150$ au, respectively. At the beginning of the calculation the disc surface density followed a power-law profile $\Sigma \propto R^{-1}$, where R is the cylindrical radius. We adopted a relatively large and massive disc as it corresponds to the kind of systems that can be observed at high spatial resolution with current instrumentation. We modelled the disc using 10^6 gas SPH particles assuming a total gas mass of $0.01\,\mathrm{M}_\odot$. We set the SPH viscosity parameter $\alpha_{\rm AV} \approx 0.26$, approximately equivalent to a mean Shakura & Sunyaev (1973) disc viscosity $\alpha_{\rm SS}$ of 0.005 (Lodato & Price 2010). We used a locally isothermal equation of state where the temperature is a function of radial distance from the disc-hosting star according to $T(r) = 64\,\mathrm{K}\,(r/r_{\rm in})^{-1/2}$. This corresponds to a disc scale height $H/R = 0.05$ at $R = R_{\rm in}$ and $H/R = 0.1$ at $R = R_{\rm out}$, consistent with recent disc observations (e.g. Pinte et al. 2016). Using an adiabatic equation of state might change the disc response as shown by Lodato et al. (2007), but we do not consider such effects in this work.

The dust content of the disc was modelled using two different methods according to the grain size considered: the one-fluid method for micron-sized grains (1–10 µm) (Price & Laibe 2015; Ballabio et al. 2018), and with dust modelled as a separate set of particles for grains between 100 µm and 10 cm (Laibe & Price 2012). We performed calculations for each grain size individually, and stacked these calculations together for radiative transfer post-processing. The dust was initialized to follow the same radial and vertical density profile as the gas, with mass scaled down by a factor of 100 from the gas mass. For further details and tests, see Paper I (section 2.2 and appendices B and C).

We considered equal-mass encounters ($q = 1$). We set the $1\,\mathrm{M}_\odot$ perturber on a parabolic orbit with initial separation 10 times the pericentre distance with $R_{\rm peri} = 200$ au. Since $R_{\rm peri} > R_{\rm out}$ this implies a non-penetrating flyby. The perturber does not have a disc previous to the encounter. We define β to be the angle between the angular momentum vector of the disc and that of the flyby orbit (see fig. 1 in Paper I). When $\beta \neq 0$ there is an additional angle between the direction of pericentre and the line of intersection of the disc and the orbital plane. We ignored this additional angle since β dominates the variation in angular momentum transfer for the dominant $m = 2$ inner Lindblad resonance in close, non-penetrating encounters (Ostriker 1994; Winter et al. 2018a). Being interested in the 3D disc structure during the flyby, we chose two representative orbits misaligned with respect to the disc mid-plane: inclined prograde ($\beta = 45^\circ$) and inclined retrograde ($\beta = 135^\circ$).

In order to build a representative disc made of a mixture of gas and dust of multiple grain sizes, we stacked the distributions of different grain size (0.1 mm, 1 mm, 1 cm, and 10 cm) following the procedure outlined in Mentiplay, Price & Pinte (2019). Since grains with sizes ranging between 1 and 10 µm are strongly coupled to the gas, we assumed that these follow the gas distribution. Therefore we ignored those calculations when stacking. We chose the gas distribution in the 0.1 mm (gas + dust) calculation as the reference for the other grain sizes. In other words, we discarded the gas from the other grain size calculations and added their dust particles to the 0.1 mm calculation. The gas distributions in each individual grain size calculations were found to be similar because of the low dust-to-gas ratio. We detail our procedure for producing synthetic observations from these simulations below.

2.2 Radiative transfer calculations

We used the stacked disc models described in Section 2.1 as input to the radiative transfer code MCFOST (Pinte et al. 2006, 2009). The radiative transfer was calculated on an unstructured Voronoi mesh derived from the SPH gas particles. Nealon et al. (2019) provide further details on the mesh construction. This allowed us to perform radiative transfer calculations on the complex geometry of

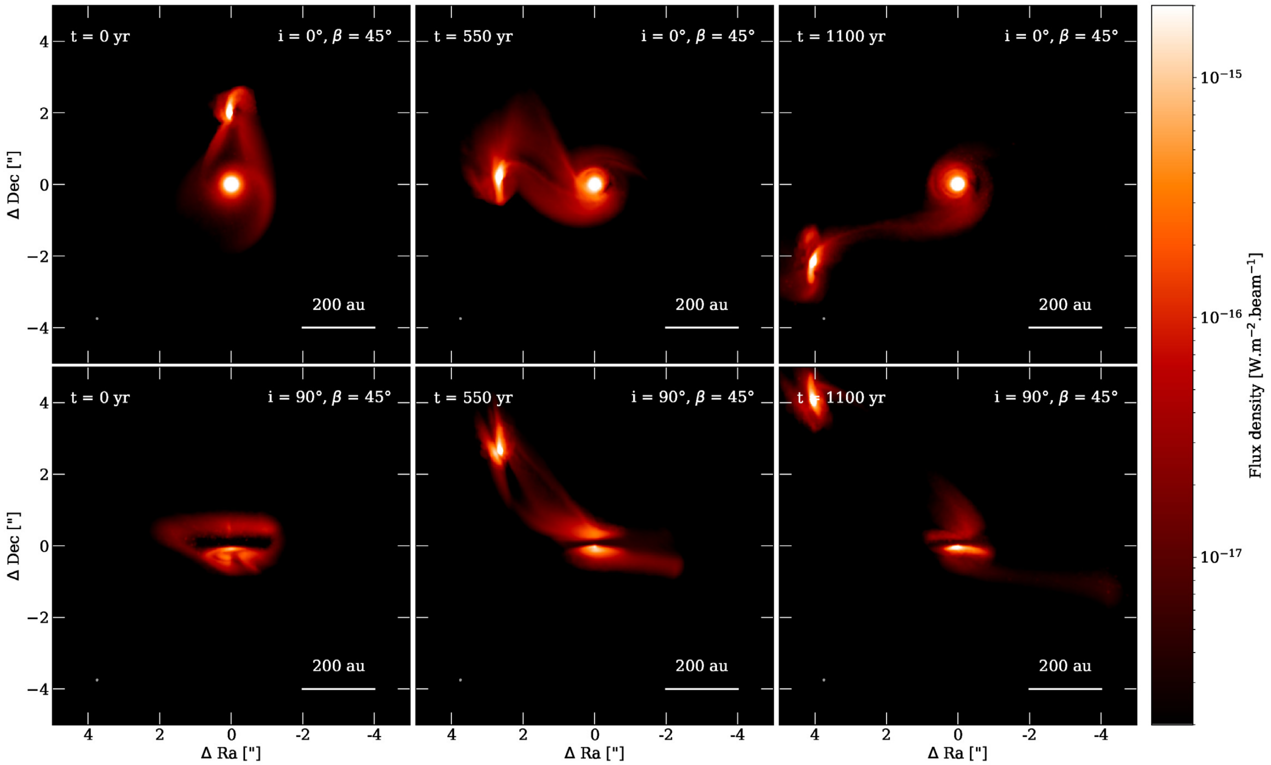

Figure 1. Disc evolution during an inclined prograde flyby ($\beta = 45°$) in scattered light ($\lambda = 1.6$ μm). A prominent bridge of material appears between the perturber and the disc. Upper row shows face-on view ($i = 0°$) while lower panel shows edge on ($i = 90°$). The beam is 50 mas × 50 mas, and is indicated by the small grey circle in the bottom left of each figure.

the perturbed disc during the flyby, without requiring interpolation between the SPH and radiative transfer codes.

We considered two sources of radiation: the central star surrounded by the disc and the perturber. This combination asymmetrically illuminates the disc (see Figs 1 and 2). Considering each star has a mass of 1 $M_\odot$, we used a stellar spectrum and luminosity derived from a 3 Myr Siess isochrone (Siess, Dufour & Forestini 2000): $T_{\rm eff} = 4262$ K, $L = 0.997\,L_\odot$, and $R = 1.722\,R_\odot$. We used 10^7 photon packets in the temperature calculation and to compute the monochromatic specific intensity. Final images were generated using a ray-tracing method (Pinte et al. 2009). Dust optical properties were computed using Mie theory, assuming astrosilicate composition (Draine & Lee 1984). For the radiative transfer, we rescaled the dust mass of each dust size bin in order to obtain a total dust-to-gas ratio of 0.01. Within each cell of the Voronoi mesh, the grain size distribution was split into 100 logarithmically spaced bins. We assumed that the spatial distribution of grains smaller than 1 μm followed the gas, i.e. the spatial distribution of modelled grain sizes did not affect the spatial distribution of small grains. The size distribution of these grains was assumed to follow a power-law $\mathrm{d}n(a) \propto a^{-3.5}\,\mathrm{d}a$. Grains between 1 μm and 0.1 mm follow the same power law such that the mass in 0.1 mm grains match the models for that grain size. For grains larger than 0.1 mm, the spatial distribution of dust with respect to the gas was determined from the output from the PHANTOM simulations. The sizes for grains between the modelled size bins were interpolated using a linear interpolation in log–log space.

We set the distance to 100 pc and the image size to 1000 au × 1000 au (equivalent to 10 arcsec × 10 arcsec). We calculated scattered light images in the *H* band at 1.6 μm, thermal emission at 850 μm, and ^{12}CO J = 3–2 molecular emission. For the CO emission we assumed a CO-to-H_2 abundance ratio of 10^{-4} (Lacy et al. 1994; France et al. 2014) and produced channel maps at 0.1 km s^{-1} resolution with a turbulent velocity of 0.05 km s^{-1}. We assumed the CO is in local thermodynamic equilibrium (as we only look at low-J CO lines) and a gas temperature equal to the dust temperature computed by MCFOST.

For direct comparison with recent observations in the sub-millimetre, we produced synthetic ALMA observations of our models with the CASA package (McMullin et al. 2007). We computed the ^{12}CO(3–2) emission (resp. continuum) at the central frequency of ~346 GHz (resp. 353 GHz) in a bandwidth of 23 MHz (resp. 600 MHz) and a spectral resolution of ~0.1 MHz (resp. 600 MHz). All the synthetic observations were done using the ‘alma.cycle10.cfg’ configuration of the interferometer and a precipitable water vapour of 0.4 mm to set the thermal noise. This resulted in a synthetic beam size of ~0.30 arcsec for both the ^{12}CO and continuum emissions (see Figs 3 and 4).

3 RESULTS

We adopt the observational convention where North is up and East is left for describing the synthetic images obtained at different wavelengths.

3.1 Scattered light

Figs 1 and 2 show scattered light synthetic observations at $\lambda = 1.6\,\mu$m for $\beta = 45°$ and $\beta = 135°$, respectively. We show three different times: when the perturber is at pericentre ($t = 0$),

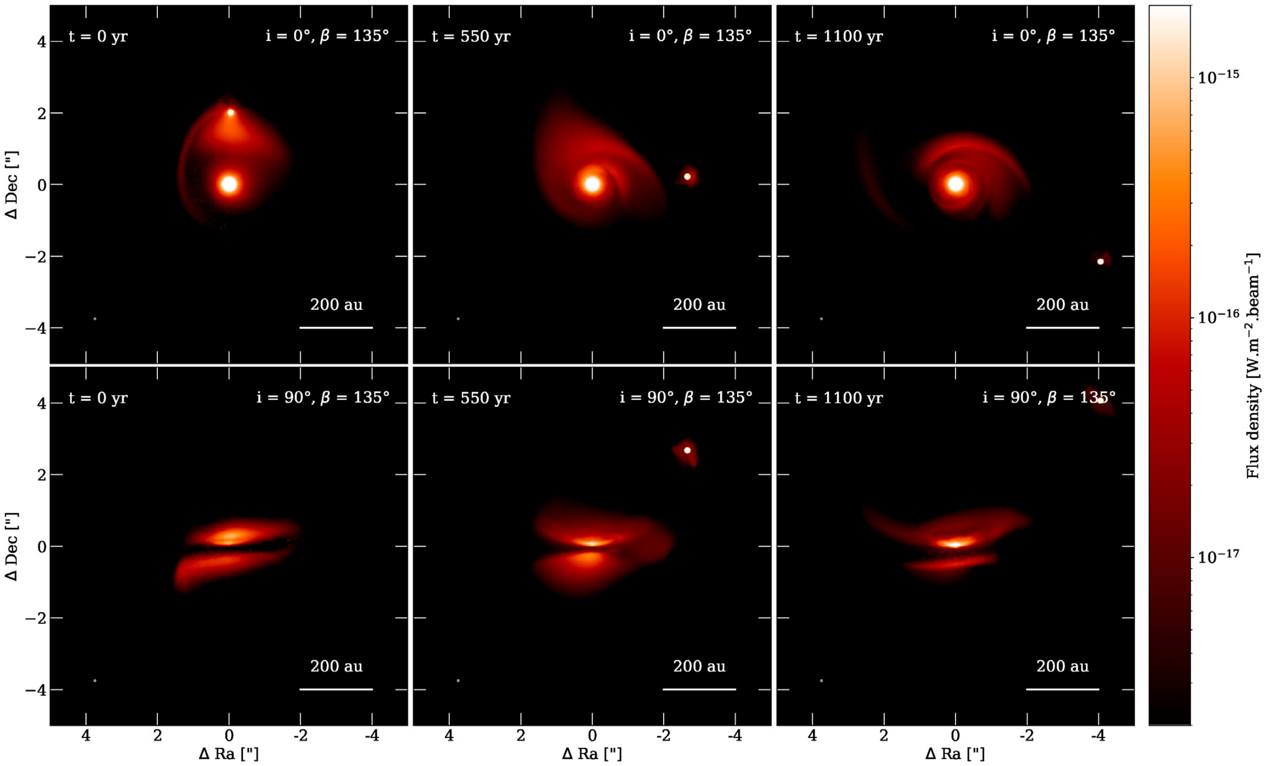

Figure 2. Same as Fig. 1 but for an inclined retrograde flyby ($\beta = 135°$). We observe a spiral arm to the North. The beam is 50 mas × 50 mas, and is indicated by the small grey circle in the bottom left of each figure.

shortly after ($t = 550$ yr) and just prior to the perturber leaving the field ($t = 1100$ yr). The three-dimensional distance between the stars is 200, 375, and 612 au (respectively). The disc is shown face on ($i = 0°$, top rows) and edge on ($i = 90°$, bottom rows) from the observer's perspective relative to the initial disc mid-plane.

The main observational difference between the prograde and retrograde encounter is the appearance of prominent spirals in the prograde case, as expected from theory (Ostriker 1994; Winter et al. 2018a). These are observed shortly after pericentre passage (middle frames in Fig. 1) where one spiral arm appears between the two stars, and the other anchored in the disc on the opposite side. Both spirals lie out of the initial disc plane.

Interestingly, the spiral arm lying between the two stars is brighter since it is simultaneously illuminated by both stars. This interstellar *bridge* remains at later evolutionary stages (see $t = 1100$ yr in the right frames of Fig. 1). Since such features are not observed for retrograde flybys, gas bridges observed in scattered light imply prograde encounters. In principle, similar bridges could also be caused by an outer bound companion, although for an unbound encounter the bridge is expected to extend over longer distances. We discuss this further in Section 4.4.

Stellar flybys also induce warps. In contrast to bridges, warps are more apparent in discs that have undergone retrograde encounters. This may be observed by comparing the disc edge-on views for $\beta = 45°$ and $\beta = 135°$ at $t = 1100$ yr (bottom right frames in Figs 1 and 2). For the retrograde flyby, the disc – initially exactly edge on – develops an asymmetric illumination between the upper and the lower parts with respect to the disc mid-plane. This is due to the disc warping caused by the flyby. As a result, after the encounter, both the far and near sides of the upper half of the disc can be seen. For instance, at $t = 1100$ yr, different illuminations between North and South exist in both the prograde and the retrograde cases. Hence, significant disc warping can be considered as a signpost of a flyby. We discuss the effect of more massive perturbers and more penetrating encounters in Section 4.1.

In line with previous works (Jílková et al. 2016; Breslau, Vincke & Pfalzner 2017; Winter et al. 2018a), we find that perturbers on prograde orbits are more efficient at acquiring material from the circumprimary disc than their retrograde counterparts. Also, since prograde encounters unbind material from smaller radii in the disc, the truncation radius is smaller for such encounters. However, the outer radius of a disc prior to encounter is not an observable quantity. Therefore, the extent of the disc in scattered light alone does not constrain encounter orientation.

All of our scattered light synthetic observations in Figs 1 and 2 closely resemble the corresponding gas density fields shown in figs 2 and 3 of Paper I. This occurs because micron-sized grains are well coupled to the gas. On the other hand, the unique shadowing patterns due to light obstruction by the disc material are only captured through radiative transfer calculations. These effects may help to constrain the disc inclination when dust continuum and kinematics are not available.

3.2 Continuum thermal emission

Fig. 3 shows the disc emission at 850 μm for $\beta = 45°$ (left column) and for $\beta = 135°$ (right column) at $t = 550$ yr. The spiral in the East in the left-hand panels of Fig. 3 corresponds to the interstellar bridge seen in scattered light (see middle column in Fig. 1). Here we show observations in face-on and edge-on configurations. Intermediate viewing inclinations (not shown) cover a broader range of pitch angles and morphologies. Shortly after periastron passage, spirals

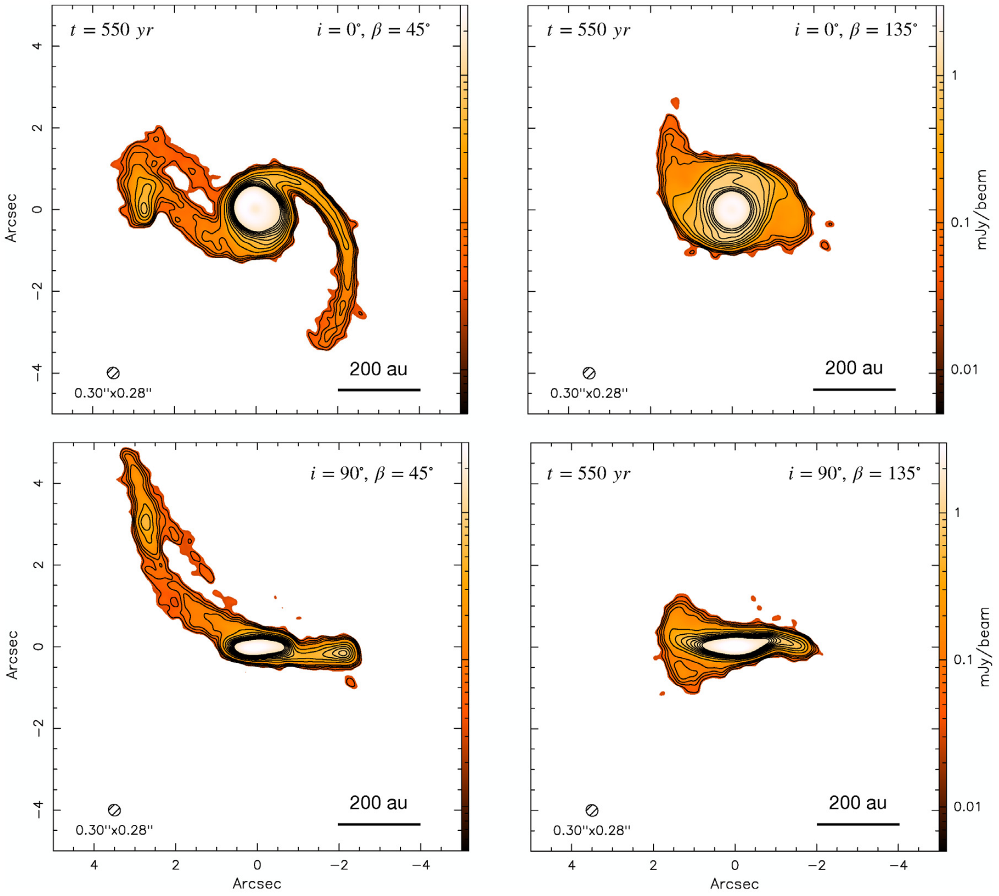

Figure 3. ALMA Band 7 synthetic observations of the thermal dust emission of the system 550 yr after the passage at pericentre for $\beta = 45^\circ$ (left column) and $\beta = 135^\circ$ (right column). The synthetic observations mimic 2 h of observation and are to be compared to the scattered light images in the middle columns of Figs 1 and 2. The top row shows the synthetic observation of the system inclined by $i = 0^\circ$ (face-on view) while the bottom row shows the system inclined by $i = 90^\circ$ (edge-on view). The contours show the level at 3σ, 5σ, 7σ and then 10σ to 100σ by step of 10σ, with $\sigma = 0.014$ mJy per beam. To ease the visualization, the data are clipped at 2σ.

exhibit large pitch angles (∼30° or more), which decrease with time. Because of projection and dynamical effects (Pfalzner 2003), the two spirals do not necessarily have the same pitch angle.

For the $\beta = 135^\circ$ case, two symmetrical spirals appear shortly after the passage at pericentre ($t = 550$ yr). These spirals appear less prominent and more compact with respect to those induced by the $\beta = 45^\circ$ encounter. As the distance between the stars increases with time, the spirals quickly disappear as the gas in the disc recircularizes. This happens in a few orbital periods at the spiral location. The continuum emission seen edge on shows a more warped geometry than the prograde encounter. This is because inclined retrograde encounters are more efficient at tilting and twisting the disc (Xiang-Gruess 2016; Cuello et al. 2019a).

For the non-penetrating encounters considered ($R_{\rm peri}/R_{\rm out} \approx 1.3$), no disc material is captured by the perturber for retrograde flybys; whereas a circumsecondary disc forms for prograde flybys. This is seen in the scattered light and continuum images. However, for more evolved discs, we expect more compact dust distributions for mm-sized grains because of radial drift (see figs 6 and 7 in Paper I). This translates into more compact spirals arms in the continuum for systems where the flyby occurs after several Myr. Therefore, for more evolved discs, the perturber only captures gas, leaving the millimetre-sized dust unaffected. This scenario is further discussed in Section 4.5 based on recent observations of interacting stellar objects. Our main result is that flyby-induced spirals (if present) are in principle detectable with ALMA in Band 7 for a reasonable integration time (∼2 h). Other bands (e.g. Band 3) and more extended configurations (i.e. higher resolution ∼0.1 arcsec) would require longer integration times.

3.3 CO kinematics

Fig. 4 shows the synthetic observations at different wavelengths for the inclined prograde $\beta = 45^\circ$ encounter taken 550 yr after the passage at pericentre. In particular, in the lower part we show the ^{12}CO(3–2) moment 0 (left) and moment 1 (right) maps. Moment 0 provides information about the distribution of gas around both stars. As already seen in scattered light images, the *bridge* of material connecting both stars is readily seen in CO moment 0. The western spiral is also detected out to separations of 5 arcsec, which is roughly twice the pericentre distance. Because of illumination effects and obscuration, this prominent spiral feature is not detected in scattered light images. However, faint spirals could be detected in the CO (Christiaens et al. 2014). Hence, CO emission lines can be used to reveal material spread around the stars during and after flybys – not seen in scattered light.

The moment 1 map in Fig. 4 provides information about the velocity field around each star in the rest frame of the host star.

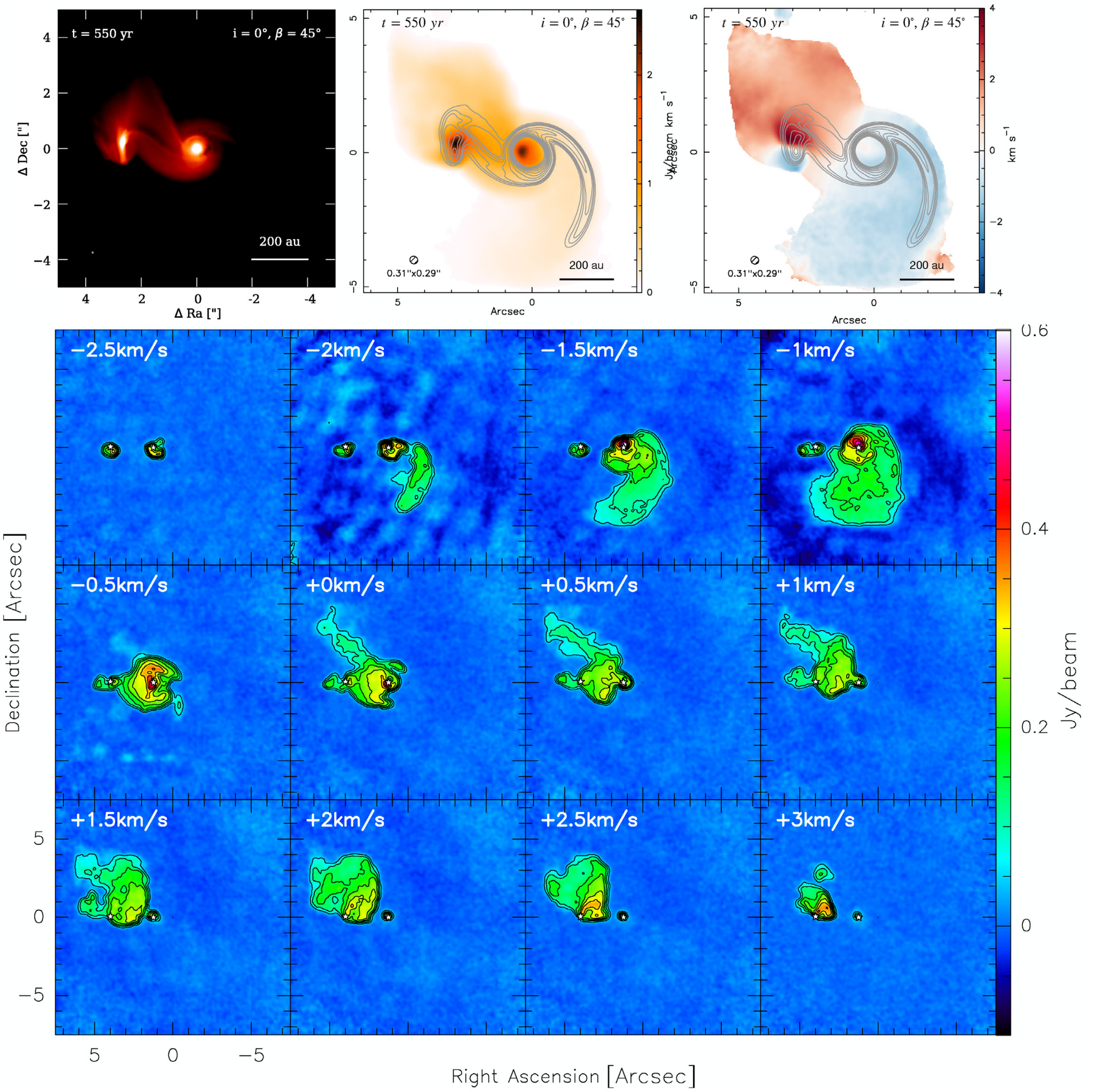

Figure 4. Observations at different wavelengths for the inclined prograde $\beta = 45°$ encounter, taken 550 yr after the passage at pericentre. Upper row: scattered light from Fig. 1 (left); moment 0 (middle), and moment 1 (right) of the ^{12}CO(3–2). The contours in grey highlight the continuum emission at 850 µm (same as the top left panel in Fig. 3). Bottom: channel maps of the ^{12}CO(3–2). The contour levels in each panel start at 5σ with 5σ steps, where $\sigma = 10.5$ mJy per Beam. The white stars indicate the location of the stars. The non-coplanar southern spiral clearly appears in the negative channels between −2 and $-0.5\,\mathrm{km\,s^{-1}}$. The perturbed disc around the primary and the bridge of material in between the two stars is seen for channels around the systemic velocity ($0 \pm 1.0\,\mathrm{km\,s^{-1}}$). This is in agreement with the scattered light emission (Fig. 1).

Within the field of view, any non-coplanar disc with respect to the plane of the sky appears as an almost symmetric region with a given spread in velocities (typically of a few $\mathrm{km\,s^{-1}}$). Hence, the features in the right-hand panel of Fig. 4 reveal evidence of both discs. The disc around the primary (although more massive and extended) has a relatively weak observational signature in moment 1 because it is almost coplanar to the plane of the sky. The disc of captured material around the perturber, being more inclined, has a larger kinematical signature, see middle column of Fig. 1. Prominent disc structures (such as spirals) translate into more asymmetric patterns in the moment 1 map. These features are however better seen by scanning through the individual channel maps.

Fig. 4 shows the ^{12}CO J = 3–2 channel maps at $0.5\,\mathrm{km\,s^{-1}}$ resolution (from +3 down to $-2.5\,\mathrm{km\,s^{-1}}$). The spiral in the south-west appears prominently across most of the negative channels from −1 up to $-2.5\,\mathrm{km\,s^{-1}}$. The width of the spiral decreases with increasing channel velocity (from systemic velocity). This is because the channels corresponding to faster velocities (e.g. $-2\,\mathrm{km\,s^{-1}}$) trace the lower disc surface while the channels for slower velocities (e.g. $-1\,\mathrm{km\,s^{-1}}$) trace the bulk of the disc instead.

The presence of the spiral across a broad range of velocities is a clear signature of non-coplanarity – see discussion in Section 4.5.4 for examples where such structures have been detected. Between -1 and $+1\,\mathrm{km\,s^{-1}}$ we see the rotation pattern of the disc around the primary plus the asymmetries due to the presence of the spiral. Since this disc is inclined only by a few degrees, the classical 'butterfly pattern' (e.g. Louvet et al. 2018) does not appear cleanly.

The disc around the perturber is inclined by approximately $\sim 80^\circ$ with respect to the plane of the sky. This explains why its rotation pattern is readily seen between $+1$ and to $+3\,\mathrm{km\,s^{-1}}$ – a coplanar disc with the plane of the sky does not produce a rotation pattern in the moment 1 map. We notice that half of the butterfly pattern appears in the positive channels (from $+1.5$ up to $+3\,\mathrm{km\,s^{-1}}$) where there is little or no overlap with the emission of the circumprimary disc. The interstellar bridge appears at velocities of about $1\,\mathrm{km\,s^{-1}}$. These kinematic signatures along with the dust continuum emission constrain the mutual inclination between the two discs. We discuss this further in Section 4.5.

4 DISCUSSION

4.1 When should you suspect a flyby?

The four main observational signatures of a stellar flyby in a protoplanetary disc are:

(i) *Spirals:* for the prograde configurations two prominent spirals appear in the disc (Clarke & Pringle 1993; Pfalzner 2003; Quillen et al. 2005). Because of projection effects and disc stripping one of these might appear as a bridge connecting both stars (see middle column of panel (a) in Fig. 1). For retrograde flybys, less prominent spirals form for misaligned orbits and almost no spirals at all for coplanar orbits (fig. 2 in Paper I). When spirals appear, these axisymmetric features efficiently trap dust. This trapping can be seen and quantified through multiwavelength observations in scattered light (Fig. 1) and in the continuum (Fig. 3). Spirals are expected to disappear over time as the disc recircularizes (in a few 1000 yr or less). As seen in fig. 2 of Paper I, the pitch angles of the two diametrically opposed spirals are not necessarily identical, and evolve over time from a few tens to several degrees. The bridge is out of the disc plane and fades more rapidly than the opposing spiral, which remains coplanar with the disc. The spirals that appear during the encounter last for a few 1000 yr (at most) for the parameters considered here. Hence, if spirals are observed in the continuum this means that the encounter must be ongoing or that the perturber is at a distance of a few thousands of au from the disc-hosting star. Given the probability of witnessing a flyby, this remains unlikely but possible none the less (see Section 4.4).

(ii) *Disc truncation:* prograde flybys result in efficient disc truncation unless $R_{\mathrm{peri}} \gg R_{\mathrm{out}}$ or $q \ll 1$ (Clarke & Pringle 1993; Ostriker 1994; Breslau et al. 2014; Winter et al. 2018a). Instead, retrograde encounters cause little or no disc truncation at all (fig. 11 in Paper I), unless the flyby is penetrating enough ($R_{\mathrm{peri}} \leq R_{\mathrm{out}}$). We find that the dust distribution in the disc is more compact than the gaseous distribution due to radial drift[1] (Weidenschilling 1977). This difference in radial extent increases with time. Therefore, during a flyby, the gaseous disc should in principle show more structure than the dusty one. In regions of high stellar density, discs can also be rapidly truncated by external photoevaporation as shown by Winter et al. (2018b). This is further discussed in Section 4.4.

(iii) *Disc warping:* a disc is referred to as warped when the angular momentum of the gas changes as a function of radius, described by the tilt and twist angles (Pringle 1996). Prograde flybys are less efficient than retrograde ones regarding disc warping (section 3.8, figs 13 and D6 in Paper I). Remarkably, retrograde inclined orbits ($\beta = 135^\circ$) cause the strongest disc tilting (Xiang-Gruess 2016) because the stripping is less severe and more material survives at larger radii. This effect is also apparent in Figs 1, 2, and 3 when comparing $\beta = 45^\circ$ with $\beta = 135^\circ$. Finally, the longevity of the warp generated by the flyby depends on the disc thickness and the outer radius of the disc (e.g. Nixon & Pringle 2010). Even after the warp dissipates, the disc will maintain its misalignment to the central star and – if observed – this could be interpreted as a signpost of a previous encounter. In that case, high-precision radial measurement of the nearby stars (as the ones obtained with *Gaia*) could help to chase the hypothetical perturber. Larger perturber masses (i.e. $q > 1$) produce more significant disc warping.

(iv) *Diffuse halo and captured material:* during a flyby, disc material can remain bound to the primary, be captured by the perturber or become unbound. For a given value of R_{peri}, the process of disc stripping is more dramatic for prograde encounters and for high values of q. This phenomenon can be detected through molecular line emission, as shown in Fig. 4 with the ^{12}CO J = 3–2 emission. For prograde (close enough) encounters, disc material is efficiently captured by the perturber. Alternatively, perturbers on retrograde orbits hardly steal material from the disc, unless $R_{\mathrm{peri}} \lesssim R_{\mathrm{out}}$. If both stars have discs previous to the encounter, then a complex exchange of material can happen between both discs. This dynamical effect is out of the scope of this work, but has potentially been observed in AS 205 for instance (see Section 4.5.2).

(v) *Dimming and extinction events:* The material that is spread around the stars during the encounter can also cause extinction. The column density along the line of sight (or equivalently the bolometric stellar flux) over time is strongly dependent on flyby parameters, disc structure, and viewing angle. This renders the dimming signature of a flyby highly degenerate. In RW Aur, such dimming events have been observed over the last years (Günther et al. 2018). For instance, in the model proposed by Dai et al. (2015), the extinction is due to the flyby-induced tidal arm (see their fig. 12). Depending on the position of the observer, the diffuse halo around the stars, the tidal arm, or the bridge of material can cause similar dimming events. This signature, although not unique and ambiguous, provides a straightforward way to identify potential systems of interest within ground-based surveys of stars.

4.2 Prograde or retrograde flyby?

In Table 1, we summarize the flyby diagnostics presented in Section 4.1. In particular, we separate each specific signature at various wavelength in prograde and retrograde cases (P and R, respectively). This provides a guide to interpret observations where a flyby is suspected. The presence of an interstellar bridge along with a diffuse halo is a signature of a prograde flyby; whereas a significantly misaligned disc is more indicative of a retrograde flyby. Multiwavelength observations (e.g. scattered light, dust continuum, and emission lines) are crucial to disentangle between both orbital orientations.

---

[1] This is especially true for the grains marginally coupled to the gas, typically of sizes ranging from 0.1 mm up to 1 cm (Laibe, Gonzalez & Maddison 2012).

Table 1. Observational signatures of flybys for different kind of observations: scattered light, dust continuum, and emission lines (e.g. CO). The symbols ∼ and × express a less robust diagnostic and the lack of information, respectively. These flyby signatures are ranked by relevance. Other mechanisms can produce similar signatures, except for bridges.

Signature	Scattered light	Dust continuum	Emission lines
Bridges	Prograde	Prograde	Prograde
Spirals	Prograde, ∼Retrograde	Prograde, ∼Retrograde	Prograde, ∼Retrograde
Disc misalignment	Retrograde, ∼Prograde	Retrograde, ∼Prograde	Retrograde, Prograde
Disc truncation	Prograde	∼Prograde	∼Prograde
Accretion event	∼Prograde	×	∼Prograde
Dust trapping	Prograde, ∼Retrograde	Prograde, ∼Retrograde	×
Diffuse halo	Prograde, ∼Retrograde	∼Prograde	Prograde, ∼Retrograde

4.3 What can we learn from the kinematics?

In Section 3.3, we described the kinematical signatures of a stellar flyby as seen in the ^{12}CO(3–2) emission line. In particular, the moment 1 map provides information about disc rotation and orientation. Assuming Keplerian rotation around each star, it is possible to obtain an estimate of the stellar masses even in the case of strongly embedded objects.

If the spectral resolution is high enough (ideally above 1 km s^{-1}), gas flowing out of the disc can be separated from the bulk of the disc. In particular, the prominent spirals generated by an inclined prograde perturber appear as arc-like features across several individual channels as shown in Fig. 4. In a configuration in which the disc is mildly inclined with respect to the plane of the sky, these two arc-like features would appear in the redshifted and blueshifted channels with respect to the $v_{\rm lsr}$ of the disc. More interestingly, if the blueshifted (respectively redshifted) channels were stacked together, the arc-like features would translate in a conical morphology. In V2775 Ori, Zurlo et al. (2017) interpreted a double cone as an evidence for a bipolar outflow, when it could be generated by two spirals out of the disc mid-plane (similar to $\beta = 45°$).

In Fig. 5, we show a sketch of disc kinematics during inclined flybys as a function of time (as seen in moment 1 CO maps for instance). The disc is initially face on and does not have any kinematical signature. Shortly after the passage at pericentre ($t > t_{\rm peri}$, left), the disc is warped and prominent spirals appear in the disc for $\beta = 45°$ and $\beta = 135°$. In the prograde case, the spirals are more radially extended and one of the spirals is seen as a bridge of gaseous material between the two stars. These spirals are not coplanar with the disc and hence have velocity departures of several km s^{-1} with respect to the systemic velocity. Spectral resolutions of the order of 1 km s^{-1} or even higher are necessary to properly map the vertical layers of the disc. Perturbers on prograde and retrograde orbits cause twist in different directions. Moreover, retrograde flybys are more efficient in tilting the disc; whereas prograde ones cause more dramatic disc truncation. These kinematical signatures are key to reconstruct the geometry of the encounter.

For a prograde flyby where disc stripping occurs and material is captured by the perturber, it is in principle possible to reconstruct the flyby geometry based on a single observation. Assuming there was no disc around the perturber prior to the encounter, the disc rotation pattern observed around the perturber constrains the orbital inclination. The moment 1 map is particularly useful in this regard to measure the relative orientation between discs. However, the problem often encountered when modelling interacting objects is that it is hard to infer the disc radial extent and disc alignment prior to the flyby. Several observations during the encounter would be ideal to restrain the (likely broad) range of possible flyby and disc configurations. However these might span over several decades or even centuries, which renders this task challenging.

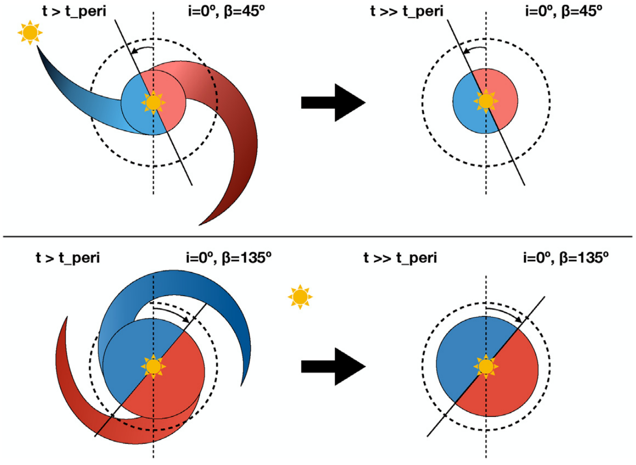

Figure 5. Disc kinematics during an inclined prograde flyby ($\beta = 45°$, top row) and an inclined retrograde flyby ($\beta = 135°$, bottom row). The disc is shown shortly after the passage at pericentre ($t > t_{\rm peri}$, left) and once the spirals and bridges have totally disappeared ($t \gg t_{\rm peri}$, right). The material in blue (red) is moving towards (away from) the observer. The colour gradients correspond to the velocity departure from the stellar systemic velocity: dark and bright correspond to fast and slow velocities. The velocity gradient increases with distance to the central star (assumed to be at systemic velocity). The dashed black line shows the radial extend of an unperturbed disc. Perturbers on prograde and retrograde orbits twist the disc in counter-clockwise and clockwise directions, respectively. Retrograde (prograde) perturbers are more efficient in tilting (truncating) the disc.

Lastly, twisted isophotes in channel maps and rotated structures in the velocity field as in Rosenfeld, Chiang & Andrews (2014) and Walsh et al. (2017) could indicate the presence of a warp in the disc. Although this has been mainly applied to circumbinary discs as HD 142527, flybys should generate similar kinematical signatures in the first moment maps of ^{12}CO (J = 3–2, J = 6–5) and HCO+(J = 4-3) for instance.

4.4 When is a flyby statistically likely?

Protoplanetary discs in the densest star-forming environments have been empirically shown to have reduced radial extents (de Juan Ovelar et al. 2012), which could be the result of flybys (Rosotti et al. 2014). However, close encounters ($R_{\rm peri} \lesssim 100$ au) between individual stars are statistically rare in regions with stellar densities $\lesssim 10^4$ stars pc^{-3}, typical of the vast majority of star-forming regions in the solar neighbourhood (Winter et al. 2018b). However, as discussed in Section 4.5, a number of such encounters have been inferred in local environments.

The resolution to this apparent paradox is that approximately half of all stars form in multiple systems (Raghavan et al. 2010). In some cases this can result in a stable binary which can influence disc evolution (Papaloizou & Pringle 1977; Daemgen et al. 2013; Kurtovic et al. 2018). In other cases, the decay of higher order multiplicity (or scattering of a third star due to the large cross-section of a binary – e.g. Hut & Bahcall 1983) can lead to the chaotic ejection of individual stars, during which particularly close encounters are possible. This is likely the case for HV Tau C and DO Tau (Winter et al. 2018c). In support of this hypothesis, Kraus & Hillenbrand (2008) find evidence of a structured spatial distribution of stars on length-scales $\gtrsim$0.04 pc in Taurus. This structure is not found on smaller scales, where it may have been erased by dynamical interactions between stars. Such a scenario is consistent with hydrodynamic simulations of star formation, which predict that encounters between stars in multiple systems are common in the early stages ($\lesssim$0.1 Myr) of cluster evolution (Bate 2018).

Since multiplicity does not appear to be strongly dependent on environment (see Duchêne & Kraus 2013 for a review), it follows that the influence of dynamical encounters on disc evolution is similarly independent of stellar clustering. This explains the apparent high occurrence rate of star–disc encounters in low-density star-forming regions. Counterintuitively, in massive and dense clusters external photoevaporation by FUV photons rapidly depletes the disc from the outer edge, such that the truncated disc may actually be less likely to be influenced by dynamical encounters (Johnstone, Hollenbach & Bally 1998; Adams et al. 2004; Facchini, Clarke & Bisbas 2016; Haworth et al. 2018; Winter et al. 2018b). Hence, while encounters do not represent an environmental mechanism for disc dispersal, they play an important role in setting their initial conditions in all stellar birth environments. They also occur almost exclusively in the early stages of cluster evolution, such that the chance of observing individual cases is low. This further motivates the theoretical exploration of encounter signatures presented here so that the small number of observed cases are understood as such.

4.5 Observed flyby candidates

The above-mentioned signatures (see Table 1) are useful to interpret systems where an ongoing (or past) flyby is suspected. We note that the repeated interaction with a bound companion generates similar dynamical signatures but more compact spirals and discs. Below we discuss a few systems of interest.

4.5.1 RW Aur

RW Aur is a system composed of two stars: RW Aur A and RW Aur B with masses of 1.4 and 0.9 $M_\odot$ (Ghez, White & Simon 1997), respectively. The presence of a prominent tidal arm observed in CO in the disc around RW Aur A (Cabrit et al. 2006) strongly suggests that RW Aur B is perturbing the disc. Dai et al. (2015) self-consistently modelled this system through hydrodynamical simulations considering a parabolic ($e = 1$), inclined ($\beta \sim 20^\circ$), and prograde encounter with $q \approx 0.64$. Moreover, RW Aur A is observed to have a high accretion rate ($\sim10^{-7}\,M_\odot\,\mathrm{yr}^{-1}$; Hartigan, Edwards & Ghandour 1995), consistent with a prograde encounter.

More recently, Rodriguez et al. (2018) reported new observations of RW Aur in the continuum and in ^{12}CO J = 2–1, at higher resolution and for larger field of view. The dust discs around both stars appear symmetrical given the beam sizes and shapes. Also, based on the presence of additional tidal streams, the authors suggest that the RW Aur system has undergone multiple flyby interactions. The radial extension of most prominent tidal arm is puzzling since several flybys would have heavily truncated the disc. Also, the likelihood of experiencing several stellar flybys during disc evolution is extremely low. In addition, several optical dimming events have been reported between 2011 and 2017, see Günther et al. (2018) for instance. These authors also report a sudden increase in Fe abundance during the event seen in X-ray emission. This feature is difficult to explain with a stream of gas passing by at a large distance. They suggest it is caused by the collision of (iron-rich) planetesimals close to the star. This would be a direct effect of the increase in eccentricity in the disc due to the perturber RW Aur B.

4.5.2 AS 205

AS 205 is multiple stellar system where two components have been resolved at 168 au projected separation. AS 205 N is a pre-main-sequence star with a mass of 0.87 $M_\odot$, and AS 205 S is a spectroscopic binary with a total mass of 1.28 $M_\odot$. The latest observations of this system reported by Kurtovic et al. (2018) show two compact discs in the continuum, one around AS 205 N and one around AS 205 S. They also reported extended emission of gas subject to complex kinematics between the two systems using ^{12}CO(2–1) emission. Remarkably, there is a bridge of gas between both sources and two spirals in the dust disc around AS 205 N. This feature strongly suggests that we are witnessing a prograde flyby with $q \approx 1.5$, where the two discs are interacting. Finally, a spiral pattern appears in the channel maps of the CO emission at around 4 km s^{-1}.

4.5.3 HV Tau and DO Tau

HV Tau is a triple system with a wide binary, HV Tau C, at ∼550 au projected separation; and a tight binary with 10 au separation. HV Tau C hosts a protoplanetary disc and it is separated by $\sim1.26 \times 10^4$ au from DO Tau, which also hosts a disc. There is a clear bridge between both source in the 160 µm emission. Winter et al. (2018c) modelled the interaction between HV Tau C and DO Tau as the decay of a quadruple system. In particular a penetrating disc–disc prograde encounter is required to unbind sufficient mass to produce the visible bridge. The mass ratio of the components is quite unconstrained, but an equal-mass encounter ($q \sim 1$) is within errors. HV Tau C additionally exhibits a high accretion rate (Woitas & Leinert 1998), also suggestive of a prograde flyby.

4.5.4 FU Ori, V2775 Ori, and Z CMa

Accretion (or equivalently outburst) events and prograde encounters are deeply connected as originally proposed by Bonnell & Bastien (1992). This mechanism could explain the stellar brightness increase of 5 or 6 mag observed in FU Ori objects. FU Ori itself is a multiple system where FU Ori N and FU Ori S have masses of 0.3 and 1.2 $M_\odot$ (Beck & Aspin 2012), respectively. FU Ori N hosts a disc and exhibits a high accretion rate that reaches values as high as of $10^{-4}\,M_\odot\,\mathrm{yr}^{-1}$. Both stellar components show compact discs in the continuum. There is also a prominent spiral out of the FU Ori N disc plane (Pérez et al., submitted), which coincides with the spiral seen in scattered light (Takami et al. 2018). This evidence strongly supports the idea that FU Ori is indeed a system experiencing a dramatic prograde flyby ($q \approx 4$).

Other recently imaged discs such as Z CMa (Takami et al. 2018), V2775 Ori (Zurlo et al. 2017), and V1647 Ori (Principe et al. 2018) exhibit suspiciously similar disc structures, along with outburst events. In Z CMa there is a prominent and open spiral arm in the disc, which could be explained by a prograde flyby in the past (Dong et al., in preparation). In V2775 Ori, in order to explain the peculiar CO emission lines, Zurlo et al. (2017) proposed a 'double cone outflow'. A prograde stellar flyby instead provides a natural explanation for the arc-like features observed in the kinematics (see for instance Fig. 4). Therefore, we suggest that a fraction of the FU Ori-like objects might be experiencing a flyby. This can be confirmed with higher resolution observations.

4.6 Caveats

The synthetic observations shown in this work correspond to the specific case of a parabolic ($e = 1$) non-penetrating flyby ($R_\mathrm{p} > R_\mathrm{out}$) between two solar mass stars ($q = 1$). Moreover, we only considered two inclinations of $\beta = 45^\circ$ (prograde) and $\beta = 135^\circ$ (retrograde). The reason why we focus on parabolic encounters is two-fold: first, as we discuss in Section 4.4, dynamical encounters between unrelated stars are rare such that the majority of star–disc encounters are expected to occur during the early stages of cluster evolution between (proto)stars in multiple stellar systems. In such interactions, encounters are by definition gravitationally focused,[2] such that $e \approx 1$. Second, star–disc encounters for which $e \approx 1$ induce the greatest angular momentum transfer and therefore generate the most prominent structures in the disc (Vincke & Pfalzner 2016; Winter et al. 2018b). More specifically, unbound perturbers on hyperbolic trajectories ($e > 1$) translate into encounters at higher velocities where the mechanism of eccentricity excitation within the disc is less significant (Winter et al. 2018b).

When calculating the kinematics, we choose a face-on view to emphasize the features generated by the non-coplanar structures identified in our simulations. A consequence of this choice is a weak signal from the primary disc, seen in Fig. 4. However, we note that even small deviations from this particular orientation will result in a measurable signal from the disc – e.g. as in TW Hya which is misaligned to the viewer by only 4° (Andrews et al. 2018; Flaherty et al. 2018; Huang et al. 2018).

Lastly, we note that we set the distance of our system at 100 pc from Earth. This is a somewhat optimistic value since the most studied star-forming regions are at distances ranging from 140 up to 400 pc. Therefore, discs in these regions would appear smaller and have lower resolution in the observations. However, even at larger distances, prominent signatures as shown in Section 3 should be readily observed.

5 CONCLUSIONS

Flybys produce remarkable and distinctive observational features at different wavelengths. By combining multiwavelength observations it is possible to reconstruct an observed flyby (perturber's orbit, disc geometry, mass ratio, and pericentre distance). Scattered light and emission lines are particularly efficient at probing the gas distribution around each of the stars and their potential misalignment. We regard these to be the most powerful diagnostics for detecting flybys. Dust continuum adds information about the flyby impact parameters.

The main observational signatures of flybys are summarized in Table 1 and are the following:

(i) Spirals and bridges: These are identified clearly in scattered light observations (Figs 1 and 2) and are more prominent for prograde encounters. Such asymmetries efficiently trap dust (Fig. 3). Additionally, misaligned encounters also leave non-coplanar kinematic signatures (e.g. CO channels, Fig. 4).

(ii) Warps and disc misalignment: Particularly for retrograde flybys, disc warping is observed in moment 1 maps (Fig. 4). Once the warp dissipates, the disc is expected to remain misaligned with respect to its host star.

(iii) Disc truncation: A more compact dust disc than gas is recovered in the observations (Fig. 3). Prograde encounters more severely truncate the disc.

Our catalogue of synthetic observations of two representative flybys provides a way to interpret recent observations of multiple objects where a flyby is suspected (see Section 4.5: RW Aur, AS 205, HV Tau and DO Tau, FU Ori, V2775 Ori, and Z CMa). Finally, the lack of bound companions in some non-axisymmetric systems – despite an active search – could be well explained by a past stellar flyby. Future observations will help to better estimate the occurrence of such encounters and understand the subsequent process of planet formation in these discs.

ACKNOWLEDGEMENTS

We thank the anonymous referee for useful suggestions. NC acknowledges financial support provided by FONDECYT grant 3170680. NC and JC acknowledge support from CONICYT project Basal AFB-170002. FL acknowledges the support of the FONDECYT program n° 3170360. This project has received funding from the European Union's Horizon 2020 research and innovation programme under the Marie Skłodowska-Curie grant agreement No 823823 (DUSTBUSTERS). CP and DJP acknowledge funding from the Australian Research Council via FT170100040, FT130100034, and DP180104235. FMe acknowledges funding from ANR of France under contract number ANR-16-CE31-0013. AJW, RN, GD, and RA acknowledge financial support from the European Research Council (ERC) under the European Union's Horizon 2020 research and innovation programme (grant agreement No 681601). JC and MM acknowledge support from Iniciativa Científica Milenio via the Núcleo Milenio de Formación Planetaria. MM acknowledges financial support from the Chinese Academy of Sciences (CAS) through a CAS-CONICYT Postdoctoral Fellowship administered by the CAS South America Center for Astronomy (CASSACA) in Santiago, Chile. LC acknowledges financial support provided by FONDECYT grant 1171246. The Geryon2 cluster housed at the Centro de Astro-Ingeniería UC was used for the calculations performed in this paper. The BASAL PFB-06 CATA, Anillo ACT-86, FONDEQUIP AIC-57, and QUIMAL 130008 provided funding for several improvements to the Geryon/Geryon2 cluster.

REFERENCES

ALMA Partnership, 2015, ApJ, 808, L3
Adams F. C., Hollenbach D., Laughlin G., Gorti U., 2004, ApJ, 611, 360
Aly H., Lodato G., Cazzoletti P., 2018, MNRAS, 480, 4738
Andrews S. M. et al., 2018, ApJ, 869, L41

---

[2] i.e. the stars have low relative velocities at infinity.

Armitage P. J., 2018, A Brief Overview of Planet Formation, Springer International Publishing AG, part of Springer Nature, p. 135
Avenhaus H., Quanz S. P., Schmid H. M., Meyer M. R., Garufi A., Wolf S., Dominik C., 2014, ApJ, 781, 87
Ballabio G., Dipierro G., Veronesi B., Lodato G., Hutchison M., Laibe G., Price D. J., 2018, MNRAS, 477, 2766
Bate M. R., 2018, MNRAS, 475, 5618
Bate M. R., Lodato G., Pringle J. E., 2010, MNRAS, 401, 1505
Beck T. L., Aspin C., 2012, AJ, 143, 55
Benisty M. et al., 2015, A&A, 578, L6
Benisty M. et al., 2017, A&A, 597, A42
Benisty M. et al., 2018, A&A, 619, A171
Boehler Y., Weaver E., Isella A., Ricci L., Grady C., Carpenter J., Perez L., 2017, ApJ, 840, 60
Bonnell I., Bastien P., 1992, ApJ, 401, L31
Breslau A., Steinhausen M., Vincke K., Pfalzner S., 2014, A&A, 565, A130
Breslau A., Vincke K., Pfalzner S., 2017, A&A, 599, A91
Cabrit S., Pety J., Pesenti N., Dougados C., 2006, A&A, 452, 897
Calcino J., Price D. J., Pinte C., van der Marel N., Ragusa E., Dipierro G., Cuello N., Christiaens V., 2019, MNRAS, 490, 2579
Casassus S. et al., 2018, MNRAS, 477, 5104
Cazzoletti P., Ricci L., Birnstiel T., Lodato G., 2017, A&A, 599, A102
Christiaens V., Casassus S., Perez S., van der Plas G., Ménard F., 2014, ApJ, 785, L12
Clarke C. J., Pringle J. E., 1993, MNRAS, 261, 190
Craig J., Krumholz M. R., 2013, ApJ, 769, 150
Cuello N., Giuppone C. A., 2019, A&A, 628, A119
Cuello N. et al., 2019a, MNRAS, 483, 4114
Cuello N., Montesinos M., Stammler S. M., Louvet F., Cuadra J., 2019b, A&A, 622, A43
Daemgen S., Petr-Gotzens M. G., Correia S., Teixeira P. S., Brandner W., Kley W., Zinnecker H., 2013, A&A, 554, A43
Dai F., Facchini S., Clarke C. J., Haworth T. J., 2015, MNRAS, 449, 1996
de Juan Ovelar M., Kruijssen J. M. D., Bressert E., Testi L., Bastian N., Cánovas H., 2012, A&A, 546, L1
Dipierro G. et al., 2018, MNRAS, 475, 5296
Dong R., Zhu Z., Rafikov R. R., Stone J. M., 2015, ApJ, 809, L5
Dong R. et al., 2018, ApJ, 860, 124
Draine B. T., Lee H. M., 1984, ApJ, 285, 89
Duchêne G., Kraus A., 2013, ARA&A, 51, 269
Facchini S., Lodato G., Price D. J., 2013, MNRAS, 433, 2142
Facchini S., Ricci L., Lodato G., 2014, MNRAS, 442, 3700
Facchini S., Clarke C. J., Bisbas T. G., 2016, MNRAS, 457, 3593
Facchini S., Juhász A., Lodato G., 2018, MNRAS, 473, 4459
Flaherty K. M., Hughes A. M., Teague R., Simon J. B., Andrews S. M., Wilner D. J., 2018, ApJ, 856, 117
France K., Herczeg G. J., McJunkin M., Penton S. V., 2014, ApJ, 794, 160
Ghez A. M., White R. J., Simon M., 1997, ApJ, 490, 353
Gratton R. et al., 2019, A&A, 623, A140
Günther H. M. et al., 2018, AJ, 156, 56
Harsono D., Alexander R. D., Levin Y., 2011, MNRAS, 413, 423
Hartigan P., Edwards S., Ghandour L., 1995, ApJ, 452, 736
Haworth T. J., Clarke C. J., Rahman W., Winter A. J., Facchini S., 2018, MNRAS, 481, 452
Hennebelle P., Lesur G., Fromang S., 2017, A&A, 599, A86
Huang J. et al., 2018, ApJ, 869, L43
Hut P., Bahcall J. N., 1983, ApJ, 268, 319
Jílková L., Hamers A. S., Hammer M., Portegies Zwart S., 2016, MNRAS, 457, 4218
Johnstone D., Hollenbach D., Bally J., 1998, ApJ, 499, 758
Keppler M. et al., 2018, A&A, 617, A44
Kraus A. L., Hillenbrand L. A., 2008, ApJ, 686, L111
Kurtovic N. T. et al., 2018, ApJ, 869, L44
Lacy J. H., Knacke R., Geballe T. R., Tokunaga A. T., 1994, ApJ, 428, L69
Laibe G., Price D. J., 2012, MNRAS, 420, 2345
Laibe G., Gonzalez J.-F., Maddison S. T., 2012, A&A, 537, A61
Langlois M. et al., 2018, A&A, 614, A88
Lesur G., Hennebelle P., Fromang S., 2015, A&A, 582, L9
Lodato G., Facchini S., 2013, MNRAS, 433, 2157
Lodato G., Price D. J., 2010, MNRAS, 405, 1212
Lodato G., Meru F., Clarke C. J., Rice W. K. M., 2007, MNRAS, 374, 590
Louvet F., Dougados C., Cabrit S., Mardones D., Ménard F., Tabone B., Pinte C., Dent W. R. F., 2018, A&A, 618, A120
McMullin J. P., Waters B., Schiebel D., Young W., Golap K., 2007, in Shaw R. A., Hill F., Bell D. J., eds, ASP Conf. Ser., Vol. 376, Astronomical Data Analysis Software and Systems XVI. Astron. Soc. Pac., San Francisco, p. 127
Mentiplay D., Price D. J., Pinte C., 2019, MNRAS, 484, L130
Montesinos M., Cuello N., 2018, MNRAS, 475, L35
Müller A. et al., 2018, A&A, 617, L2
Nealon R., Dipierro G., Alexander R., Martin R. G., Nixon C., 2018, MNRAS, 481, 20
Nealon R., Pinte C., Alexander R., Mentiplay D., Dipierro G., 2019, MNRAS, 484, 4951
Nixon C. J., Pringle J. E., 2010, MNRAS, 403, 1887
Ostriker E. C., 1994, ApJ, 424, 292
Papaloizou J., Pringle J. E., 1977, MNRAS, 181, 441
Pérez L. M. et al., 2016, Science, 353, 1519
Pfalzner S., 2003, ApJ, 592, 986
Pfalzner S., 2013, A&A, 549, A82
Pinte C., Ménard F., Duchêne G., Bastien P., 2006, A&A, 459, 797
Pinte C., Harries T. J., Min M., Watson A. M., Dullemond C. P., Woitke P., Ménard F., Durán-Rojas M. C., 2009, A&A, 498, 967
Pinte C., Dent W. R. F., Ménard F., Hales A., Hill T., Cortes P., de Gregorio-Monsalvo I., 2016, ApJ, 816, 25
Pinte C. et al., 2018, ApJ, 860, L13
Pinte C. et al., 2019, Nat. Astron., 419
Poblete P. P., Cuello N., Cuadra J., 2019, MNRAS, 489, 2204
Price D. J., Laibe G., 2015, MNRAS, 451, 813
Price D. J. et al., 2018a, PASA, 35, e031
Price D. J. et al., 2018b, MNRAS, 477, 1270
Principe D. A. et al., 2018, MNRAS, 473, 879
Pringle J. E., 1996, MNRAS, 281, 357
Quillen A. C., Varnière P., Minchev I., Frank A., 2005, AJ, 129, 2481
Raghavan D. et al., 2010, ApJS, 190, 1
Rodriguez J. E. et al., 2018, ApJ, 859, 150
Rosenfeld K. A., Chiang E., Andrews S. M., 2014, ApJ, 782, 62
Rosotti G. P., Dale J. E., de Juan Ovelar M., Hubber D. A., Kruijssen J. M. D., Ercolano B., Walch S., 2014, MNRAS, 441, 2094
Shakura N. I., Sunyaev R. A., 1973, A&A, 24, 337
Siess L., Dufour E., Forestini M., 2000, A&A, 358, 593
Stolker T. et al., 2016, A&A, 595, A113
Takami M. et al., 2018, ApJ, 864, 20
Tsukagoshi T. et al., 2016, ApJ, 829, L35
Vincke K., Pfalzner S., 2016, ApJ, 828, 48
Walsh C., Daley C., Facchini S., Juhász A., 2017, A&A, 607, A114
Weidenschilling S. J., 1977, MNRAS, 180, 57
Winter A. J., Clarke C. J., Rosotti G., Booth R. A., 2018a, MNRAS, 475, 2314
Winter A. J., Clarke C. J., Rosotti G., Ih J., Facchini S., Haworth T. J., 2018b, MNRAS, 478, 2700
Winter A. J., Booth R. A., Clarke C. J., 2018c, MNRAS, 479, 5522
Woitas J., Leinert C., 1998, A&A, 338, 122
Xiang-Gruess M., 2016, MNRAS, 455, 3086
Zhu Z., 2019, MNRAS, 483, 4221
Zurlo A. et al., 2017, MNRAS, 465, 834
van der Marel N. et al., 2013, Science, 340, 1199
van der Plas G. et al., 2019, A&A, 624, A33

This paper has been typeset from a TeX/LaTeX file prepared by the author.